ADVANCED MATERIALS
www.advmat.de

Reconfigurable Liquid Crystal-Based Physical Unclonable Function Integrating Optical and Electrical Responses

Hee Seong Yun, Dayan Wei, Sungjun Yang, Geonhyeong Park, Min Seok Kim, Tae Joo Shin, David M. Walba, Moon Jong Han, and Dong Ki Yoon**

Physical unclonable functions (PUFs)—a hardware-based security device using randomness—have evolved from basic integrated circuit designs to advanced systems using diverse materials and mechanisms. However, most PUFs are limited by single-factor challenges and fixed key generation, making them vulnerable to brute-force attacks. A reconfigurable and multidimensional liquid crystal (LC)-based PUF is presented integrated into an organic field-effect transistor (OFET) to address limitations. This system combines optical and electrical PUFs through unique optical fingerprint textures and random molecular alignment of the semiconductive smectic LC material. The PUF can be reconfigured by a simple heating and cooling process, overcoming the limitations of fixed-structure PUFs. Furthermore, this approach enhances security by enabling hierarchical authentication due to the multi-response factors, providing robust solutions for anticounterfeiting and cryptographic applications.

1. Introduction

The need for secure and reliable anticounterfeiting solutions has become increasingly critical with the rapid development of the Internet of Things (IoT).[1–3] While software-based security systems are widely used, they rely on digital algorithms and stored data, making them susceptible to attacks such as side-channel analysis and reverse engineering.[4–6] Physical unclonable functions (PUFs) have emerged as a significant advancement in security, offering solutions to these limitations. PUFs utilize microscopic uncertainties generated during manufacturing or the intrinsic disorder in natural systems to create unique and consistent responses that are unpredictable yet reproducible.[7–12] These properties make PUFs highly suitable for various applications, including device authentication, cryptographic key generation, and random number generation.[8,10–12] Over time, PUFs have evolved from basic integrated circuit-based designs to more advanced systems that employ diverse materials and physical mechanisms, such as optical and electrical principles.[8–13] Optical PUFs rely on light interactions—scattering, reflection, or transmission—through micro- and nanoparticles,[14–25] polymers,[26–31] liquid crystals (LCs),[32–35] and biomaterials,[36–38] while electrical PUFs exploit electrical properties such as charge mobility, current, and threshold voltage in field-effect transistors (FETs),[39–42] and they also rely on current and resistance in nanomaterials.[30,43–45]

Despite these advancements, conventional PUFs often rely on a single type of challenge for response generation, limiting the number of keys and increasing susceptibility to brute-force attacks.[14,15,17–24,26–29,31,32,34–39,41–44] These limitations are addressed by integrating optical and electrical PUFs into a multidimensional and reconfigurable system that enhances security and adaptability—allowing users to choose and use their preferred authentication method. Multidimensional PUFs provide flexibility by allowing optical PUFs to replace electrical ones in

H. S. Yun, G. Park, D. K. Yoon
Department of Chemistry
Korea Advanced Institute of Science and Technology (KAIST)
Daejeon 34141, Republic of Korea
E-mail: nandk@kaist.ac.kr

D. Wei, D. M. Walba
Department of Chemistry and Soft Materials Research Center
University of Colorado
Boulder, CO 80309, USA

The ORCID identification number(s) for the author(s) of this article can be found under https://doi.org/10.1002/adma.202504288

DOI: 10.1002/adma.202504288

S. Yang
UNIST Central Research Facilities
Ulsan National Institute of Science and Technology (UNIST)
50 UNIST-gil, Ulsan 44919, Republic of Korea

M. S. Kim
School of Electrical Engineering and Computer Science
Gwangju Institute of Science and Technology (GIST)
Gwangju 61005, Republic of Korea

T. J. Shin
Graduate School of Semiconductor Materials and Devices Engineering
Ulsan National Institute of Science and Technology (UNIST)
50 UNIST-gil, Ulsan 44919, Republic of Korea

M. J. Han
Department of Semiconductor Engineering
Gachon University
Seongnam 13120, Republic of Korea
E-mail: doorbell1@gachon.ac.kr

power-constrained or electrically unstable environments. In contrast, electrical PUFs can substitute optical systems where complex optical setups are impractical. Reconfigurability further enhances security by generating infinite unique responses from a single device, offering effective countermeasures against key exposure.[46] Recent studies on reconfigurable optical PUFs have primarily focused on utilizing phases or structural changes induced by thermal stimuli. Park et al.[33] and Nocentini et al.[34] implemented systems based on structural variations observed in POM images, which arise from phase transitions in LCs under different temperatures. Gan et al.[47] and Yang et al.[48] demonstrated reconfigurable optical PUFs by exploiting changes in speckle patterns resulting from thermally induced structural rearrangements in nanocrystals. For electrical PUFs, reconfigurability is typically achieved through voltage-driven transformations of electrical or magnetic properties. For instance, Shao et al.[49] utilized the memristive properties of graphene to modulate current in FETs, while Dodda et al.[50] applied voltage-controlled magnetic anisotropy to induce random transitions between parallel and antiparallel magnetic states in nanoscale magnetic tunnel junction arrays. Although various approaches to reconfigurable PUFs have been proposed, achieving integration of optical and electrical PUFs is challenging due to the challenge of designing a system that supports optical and electrical responses simultaneously without interference and crosstalk while being a reconfigurable materials. Overcoming these challenges requires innovative approaches to material design and device engineering to unlock the full potential of advanced PUF systems.

We fabricate a reconfigurable and multidimensional LC-based PUF in this work using an organic field-effect transistor (OFET) approach. The benzothieno[3,2-b][1]benzothiophene (BTBT)-derivative semiconducting LC material exhibits a phase sequence of smectic A (SmA), smectic E (SmE), and crystalline (Cr) phases upon cooling from the isotropic (Iso) phase at 208 °C. Random nucleation occurs during the Iso-to-SmA phase transition, while the SmA-to-SmE transition produces a characteristic fingerprint texture with randomly distributed skeletal patterns, including ending and bifurcation points, which serve as an optical PUF. Simultaneously, the randomly aligned molecules in the OFETs generate unpredictable electrical characteristics independently—such as threshold voltage, charge mobility, on-current, and subthreshold slope—that function as an electrical PUF. The performance of optical and electrical PUFs, including randomness, uniqueness, and reliability, is verified through statistical analyses. It is confirmed that the thermotropic LC-based fingerprint patterns can be reconfigured through facile heating and cooling cycles without correlation to the original patterns. We highlight the potential of our strategy to achieve multidimensionality and reconfigurability within a single PUF device through a system with diverse optical and electrical responses designed to enhance security and adaptability (**Table 1**). Notably, diverse response factors from a single semiconducting LC material without interference between optical and electrical responses enhance adaptability, reliability and encoding capacity. Moreover, the incorporation of reconfigurable properties strengthens security by allowing the generation of new and unique keys from the same physical device, enabling recovery from key exposure without the need for hardware replacement. As a result, our strategy enhances security and functionality, offering a robust solution for a wide range of security applications.

2. Results and Discussion

2.1. Generation of PUF

The strategy for PUF generation based on LC to realize reconfigurable and multidimensional properties is shown in **Figure 1**. First, a LC organic semiconductor (LC OSC) of the BTBT series, 2-(2,3-difluorophenyl)-7-octyl-[1]benzothieno[3,2-b][1]benzothiophene (2FPh-BTBT-C8), was synthesized by modifying a previously established synthetic route (Figure 1a; Figure S1, Supporting Information).[52] Polarized optical microscopy (POM) is used to investigate the origin of the optical fingerprint texture observed in the Cr phase of 2FPh-BTBT-C8 film, confirming the presence of SmA, SmE, and Cr phases during the cooling process (Figures S2 and S3, Supporting Information). Upon cooling from the Iso phase, 2FPh-BTBT-C8 transforms into the SmA phase, which results in a fan-shaped texture in a random manner (Figure S3a, Supporting Information). The phase transition from SmA to SmE produces a unique fingerprint texture due to the herringbone arrangement of molecules (Figure S3b, Supporting Information).[52–55] Even when the 2FPh-BTBT-C8 film transitions from the SmE to the Cr phase, the fingerprint pattern remains intact, allowing the observation of the optical fingerprint pattern using a POM (Figure S3c and Video S1, Supporting Information).

To generate optical and electrical PUFs simultaneously, using the fingerprint patterns of 2FPh-BTBT-C8 films, we developed OFET to harness the LC semiconductor's orientation-dependent electrical properties. The schematic illustrations and device structure of the OFET are shown in Figure S4 (Supporting Information). For bottom-gate bottom-contact configuration of OFET devices, planar anchoring polyimide (PAPI), serving as both a planar degenerate alignment and a dielectric layer, was first coated onto an indium-tin-oxide (ITO) glass substrate. Au/Ti electrodes were sequentially deposited by thermal evaporation through a metal shadow mask. Finally, a prepared PAPI-coated top glass substrate was combined with the bottom substrate using UV glue and the 4 μm silica bead to generate a uniform cell gap. 2FPh-BTBT-C8 powder was injected between the top and bottom substrates via capillary action near the Iso phase transition temperature and cooled to the Cr phase.

The random orientation of 2FPh-BTBT-C8 enables the realization of multidimensional—optical and electrical—PUFs. The ending and bifurcation points extracted from the random fingerprint pattern through image processing of optical microscope images can be used in optical PUFs. (Figure 1c). The optical PUF key generation process was conducted using customized MATLAB codes, as detailed in Figure S7 (Supporting Information). Additionally, anisotropic LC OSCs exhibit varied charge transport pathways depending on the alignment direction.[52,54,56] As a result, the random orientation of the 2FPh-BTBT-C8 between the source and drain provides unique electric characteristics for each device, thereby enabling the generation of an electrical PUF. Our single PUF sample consists of 4 × 6 OFET devices (Figure S4b, Supporting Information), and electrical characteristics were mapped from each device. By defining a threshold

Table 1. Comparisons of the functionality of different types of PUFs.

Materials	Types	Reconfigurability	Encoding capacity	Number of response factors[a] that can be produced with one material[b]
Fluorescent particles[22]	Optical	No	$\approx 2^{40}$ / 200 × 200 μm^2	1 (Intensities of fluorescence signals)
Fluorescent particles[24]	Optical	No	$\approx 2^{120}$ / 7 × 7 mm^2	1 (Intensities of fluorescence signals)
Raman particles[16]	Optical	No	$\approx 2^{334}$ / 40 × 40 μm^2	1 (Intensities of Raman scattering)
Raman particles[18]	Optical	No	$\approx 2^{50\,000}$ / 100 × 100 μm^2	1 (Intensities of Raman scattering)
Cholesteric LC[33]	Optical	Yes (irreversible)	$\approx 2^{184}$ / 640 × 640 μm^2	1 (Structures of the cholesteric finger)
Polymer-stabilized LC[34]	Optical	Yes (reversible)	$\approx 2^{1\,750}$ / 1 × 1 cm^2	1 (Speckle pattern)
Stochastic crystallization of a supersaturated sodium acetate solution[51]	Optical	Yes (irreversible)	$\approx 2^{541}$ / 28 × 28 μm^2	1 (Speckle pattern)
VO_2 nanocrystal[47]	Optical	Yes (reversible)	$\approx 2^{655\,360}$ (unknown size)	1 (Speckle pattern)
$Ge_2Sb_2Te_5$ nanocrystal[48]	Optical	Yes (irreversible)	$\approx 2^{4\,147\,200}$ / cm^2	1 (Speckle pattern)
Metal oxide thin film transistors[42]	Electrical	No	$\approx 2^{200}$ / 2 × 2 cm^2 (each electrical parameter)	5 (5 OFET parameters)
Graphene field-effect transistors[50]	Electrical	Yes (reversible)	$\approx 2^{64}$ / 0.5 μm^2	1 (Source-drain current)
Block copolymer nanostructure[30]	Optical and electrical	No	$\approx 2^{15}$ / 200 × 200 μm^2 (electrical), 2^{15} / 50 × 50 μm^2 (dichroism), 2^{15} / 0.75 × 0.75 μm^2 (Raman), 2^{119} / 1 × 1 μm^2 (nano-morphology)	4 (Electrical conductivity, optical dichroism intensity, and Raman scattering intensity, and morphology of nanostructure)
Zinc oxide particles[45]	Optical and electrical	No	$\approx 2^{1\,024}$ / 48 × 48 μm^2 (optical), $2^{1\,024}$ / 1.5 × 1.5 mm^2 (electrical)	2 (Optical pattern and electrical resistance)
This work	Optical and electrical	Yes (irreversible)	$\approx 2^{5\,700}$ / 432 × 144 μm^2 (optical), 2^{96} / 1.5 × 1.5 cm^2 (electrical)[c]	8 (Optical: ending, bifurcation, and 2 birefringent intensities, electrical: 4 OFET parameters)

[a] The "number of response factors" refers to how many distinct types of responses can be obtained from a single PUF. In our work, as shown in c, one PUF provides a total of eight different codes: ending, bifurcation, threshold voltage, mobility, on-current at $V_{GS} =$ −50 V, subthreshold slope, and two types of octal codes extracted from POM images. Therefore, the number of response factors in our case is eight. As another example, the reference on block copolymer nanostructures reports four types of binary codes based on randomized electrical conductivity, optical dichroism intensity distribution, Raman scattering intensity, and morphology of nanostructure.[30] Thus, the number of response factors in that study is four. [b] The method of expanding the pixel numbers or bases is not reflected. [c] Encoding capacity of optical PUFs is calculated by multiplication of encoding capacities of ending, bifurcation, and two types of octal codes extracted by polarized optical microscopy images, and that of electrical PUFs is calculated by multiplication of encoding capacities of threshold voltage, mobility, on-current at $V_{GS} =$ −50 V, and subthreshold slope binary codes, presented in Figure 6c.

value, an electrical binary PUF key was generated (Figure 1d). Furthermore, PUF demonstrates reconfigurability due to the LC phase of 2FPh-BTBT-C8, a crucial feature that enhances the security of the PUFs, which is not easy to rationalize in previous studies.[14–31,34–37,39–45] During heating to the Iso phase followed by cooling to the Cr phase, 2FPh-BTBT-C8 loses its original molecular orientation. It forms a new fingerprint texture different from before (Figure 1b), thereby generating unique optical and electrical PUFs (Figure 1e). This reconfigurability in the PUF is essential for overcoming the limitations of complexity, cost, integration, and tampering in various applications.

2.2. Analysis of Optical and Electrical Characteristics According to the Cooling Rate

LC OSCs' domain size and microstructure vary with the cooling rate, impacting optical texture and charge transport pathways.[57,58] Therefore, it should exhibit sufficient optical complexity with varied electrical characteristics for PUF. The optical images and electrical characteristics of 2FPh-BTBT-C8 films prepared under four cooling rate conditions (quenching, 20, 5, and 1 °C min^{-1}) are investigated to rationalize our idea (**Figure 2**). Under quenching conditions, the domain size of the needle texture is smaller, and the density of the dark area due to defects becomes larger compared to other slower cooling rates (Figure 2a,e). These results indicate that obtaining fingerprint patterns is challenging from the 2FPh-BTBT-C8 film under quenching conditions, making it unsuitable for optical PUF use. Moreover, the crystal domain size decreases due to insufficient time for ordering under quenching,[57] leading to the lowest charge mobility of 0.1021 cm^2 V^{-1} s^{-1} (Figure 2i and **Table 2**). As the cooling rate decreases from 20 to 1 °C min^{-1}, the domain size and charge mobility increase, and defect density decreases (Figure 2b–d,f–h,j–l, and Table 2). Powder X-ray diffraction (PXRD) experiment was performed to investigate the crys-

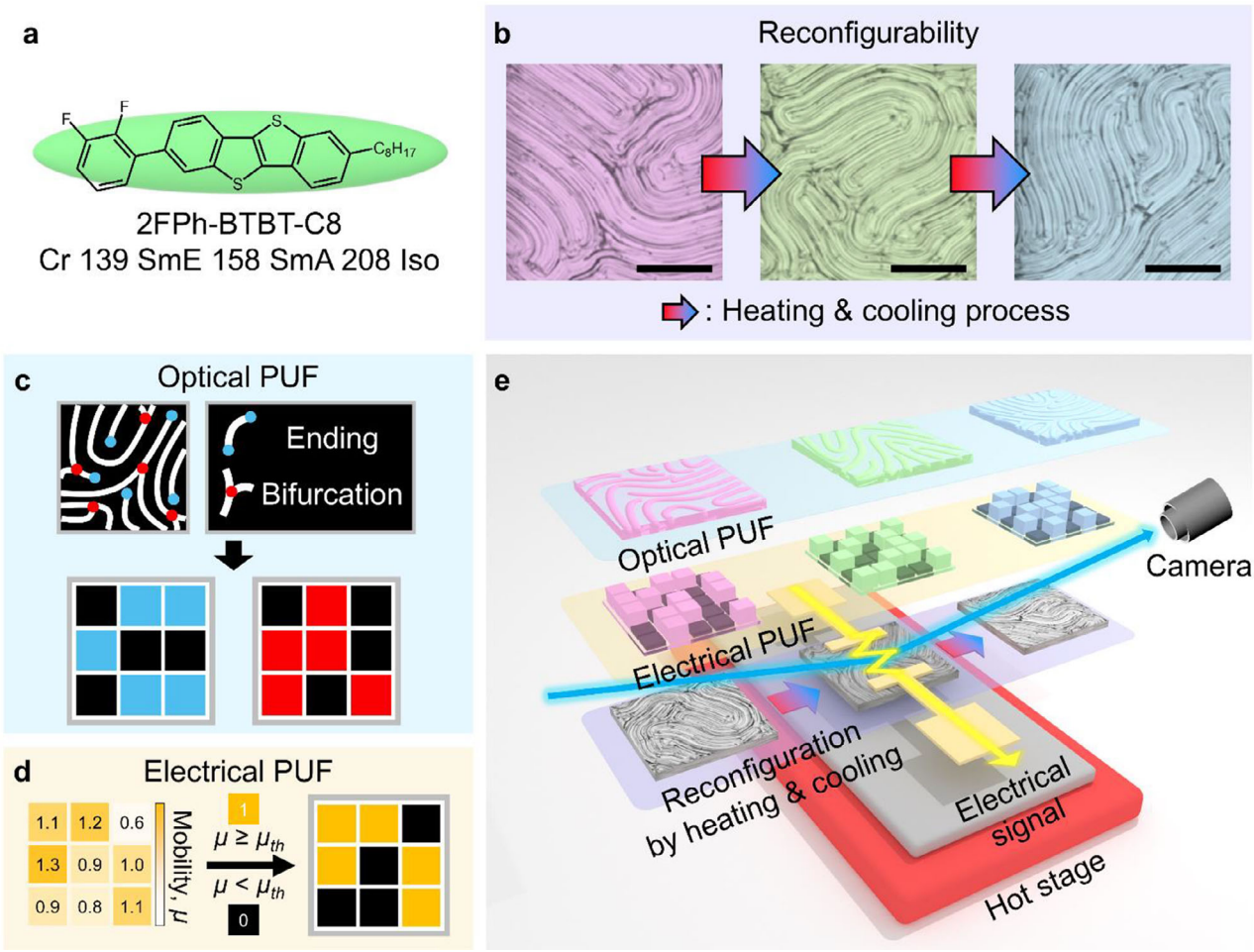

Figure 1. Reconfigurable and multidimensional LC-based PUF. a) LC molecular structure for fabricating PUF. b) Reconfigurable optical fingerprint textures of the LC film at the Cr phase by heating and cooling process. The images are colored for easier understanding of reconfigurability. Scale bars, 50 μm. c) Optical PUF is generated by converting fingerprint pattern to fingerprint skeleton and defining ending and bifurcation points. d) Electrical PUF is generated by measuring randomly distributed electrical signals of randomly oriented 2FPh-BTBT-C8 molecules. e) Schematic illustration of PUF. Reconfigured pattern generates unique optical and electrical PUFs which are distinct from the previous ones.

talline structure of 2FPh-BTBT-C8. The possible unit cell parameters and space group of 2FPh-BTBT-C8 are determined using EXPO software[59] and refined through whole pattern profile matching with the LeBail method.[60] The refined structure of 2FPh-BTBT-C8 corresponds to an orthorhombic crystal system (Pmm2 space group) with parameters: a = 4.5722 Å, b = 6.0291 Å, c = 47.1158 Å, and $\alpha = \beta = \gamma = 90°$ (Figure S5, Supporting Information). Synchrotron 2D grazing incidence X-ray diffraction analyses were performed to investigate the molecular ordering of 2FPh-BTBT-C8 under different cooling rates. Under cooling rates of 20, 5, and 1 °C min^{-1}, nucleation and growth occur through thermodynamic control. In contrast, kinetic control takes over during quenching, cooling rates are close to 100 °C s^{-1}, which leaves little time for molecules to organize into a well-ordered layered structure, resulting in the absence of high-order (00l) peaks (Figure S6a–c, Supporting Information). Especially, the attenuated intensity at q = 0.12 – 0.25 $Å^{-1}$, in the q_z line cut under quenching conditions indicates a distribution in the layer spacing, suggesting that molecules fail to achieve a consistent layered arrangement (Figure S6c, Supporting Information).[57] Consequently, charge mobility is reduced, and a large fingerprint pattern does not emerge. Furthermore, the horizontal (002) peak is more dominant than the vertical (002) peak in quenching conditions, corresponding to the vertically aligned layers with face-on molecules (Figure S6d, Supporting Information). However, as the cooling rate decreases, the vertical peak becomes increasingly dominant, reflecting the thermodynamic stability of the horizontally aligned layer. This alignment enhances charge transport and results in a larger fingerprint pattern. It indicates that although edge-on and face-on orientation of molecules coexist at slow cooling rates (Figure S6e, Supporting Information), the domain size of the fingerprint pattern is strongly influenced by the fraction of edge-on aligned molecules. From the perspective of FETs, a single and large domain or crystal is considered optimal for efficient charge transport. However, this is practically unfeasible, and regions with edge-on aligned molecules may present between domains. As the cooling rate becomes slower, it is speculated that the mixed orientation exhibits $\pi-\pi$ stacking in both in-plane and out-of-plane directions, forming a continuous 3D charge transport

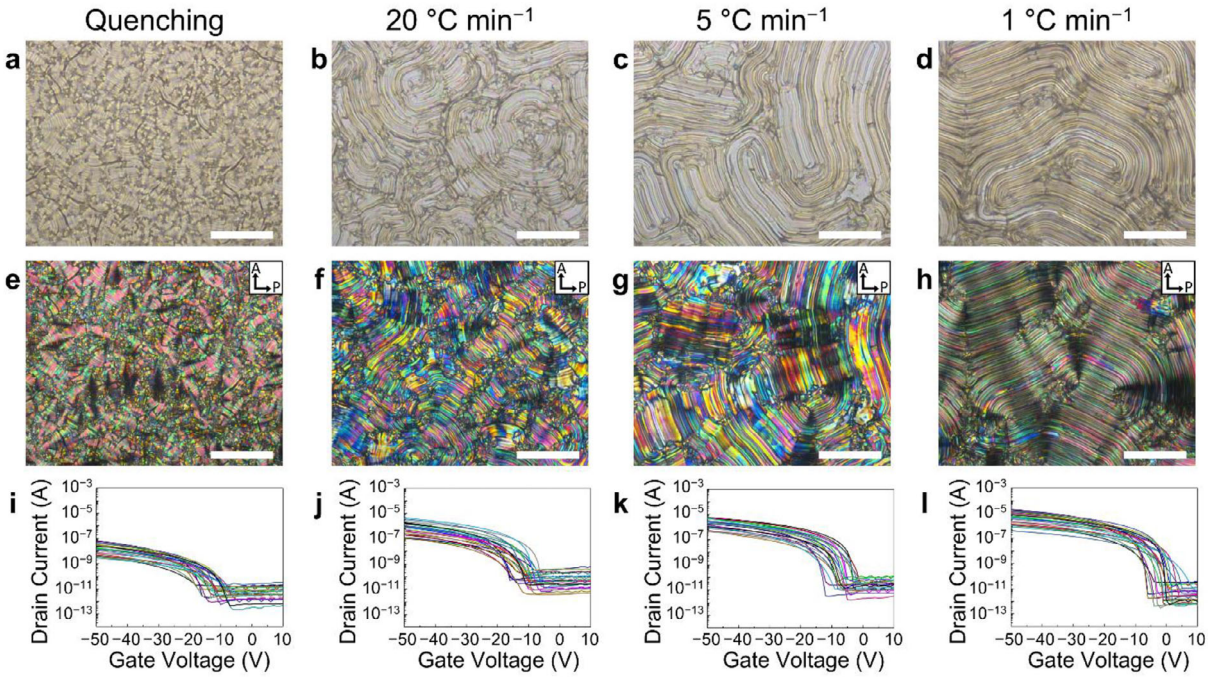

Figure 2. Optical textures and electrical characteristics of PUF depending on the cooling rate. a–d) Optical fingerprint textures and e–h) POM images depending on the cooling rate and i–l) corresponding transfer curves. Transfer curves containing 24 measurements for each cooling rate. All scale bars, 50 μm.

pathway in the film and enhancing charge hopping to the adjacent domain to achieve a higher charge carrier mobility.[61,62] For electrical PUF, we utilized the electrical anisotropy characteristics induced by the orientation of LC [52,54,56,63,64] to intentionally generate electrical randomness by inducing random π–π stacking direction and source/drain direction through random alignment. While randomness is essential from the perspective of electrical PUF, excessive electrical randomness can degrade the reliability of electronic devices, making variation reduction necessary. The following are strategies to reduce electrical variability: 1) Downsizing the source/drain channel dimension to the present domain size to reduce the possibility of charge trapping at grain boundaries.[65,66] 2) Introducing the self-assembled monolayer as contact interlayer between metal and OSC layer to alleviate the contact limitation and tune the charge injection, roughness, and trap density.[67,68] 3) Reducing the size of the spacers between the top and bottom substrates of the present sandwich cell reduces the thickness of OSC layer and minimizes the contact resistance and traps for charges.[69,70]

Based on the POM and GIXD results, a cooling rate of 5 °C min^{-1} is adopted for PUF fabrication due to the appropriate domain size and complexity of fingerprint textures. A rate of 1 °C min^{-1}, although yielding the highest charge mobility, is not chosen due to the relatively long-range orientation of the domains, which reduces the randomness of the optical fingerprint pattern. All samples used in the statistical evaluation of PUFs to be described later are fabricated at a cooling rate of 5 °C min^{-1}. LC OSCs' cooling rate-dependent random molecular ordering and orientation indicate concealable properties of the present combined optical and electrical PUFs, which can encrypt and decrypt the random codes more multidimensionally and allow the dynamic control of micro-fingerprint pattern generation.

2.3. Statistical Evaluation of the Performance for Optical PUF

We evaluated the performance and reliability of 72 optical PUFs generated by random fingerprint patterns (**Figure 3**). As shown

Table 2. The electrical characteristics of devices depending on the cooling rates. The mean and standard deviation were obtained from 24 different OFET devices.

Electrical characteristics	Quenching	20 °C min^{-1}	5 °C min^{-1}	1 °C min^{-1}
Threshold voltage, V_{th} (V)	−29.17 ± 4.11	−27.83 ± 3.83	−23.83 ± 5.02	−18.71 ± 5.34
Mobility, μ (cm^2 V^{-1} s^{-1})	0.1021 ± 0.0813	0.6847 ± 0.3789	0.7298 ± 0.4500	0.8932 ± 0.6246
On-current at V_{GS} = −50 V, I_{DS} (A)	$2.03 \times 10^{-8} \pm 1.64 \times 10^{-8}$	$1.09 \times 10^{-6} \pm 1.04 \times 10^{-6}$	$2.45 \times 10^{-6} \pm 1.73 \times 10^{-6}$	$1.89 \times 10^{-5} \pm 1.63 \times 10^{-5}$
Subthreshold slope, S-slope (V dec^{-1})	4.36 ± 0.97	3.82 ± 1.00	3.60 ± 0.98	3.47 ± 0.85

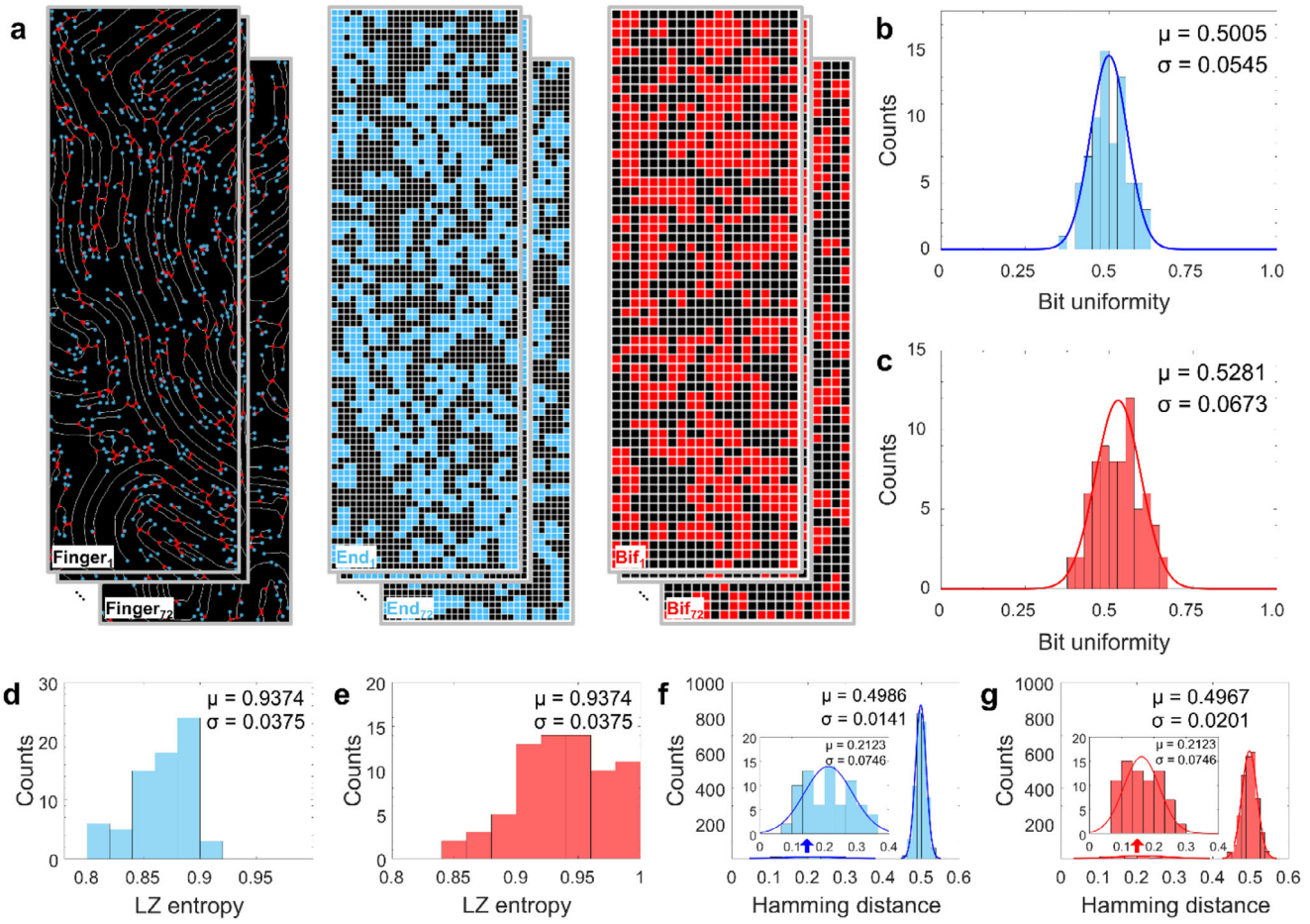

Figure 3. Generated 2D binary optical PUF keys and evaluation of PUF performance by statistical analysis. a) Generated optical fingerprint images, ending keys, and bifurcation keys. Ending key has 30 × 90 bits, and bifurcation key has 20 × 60 bits. b,c) Bit uniformity histograms with Gaussian fittings of the (b) ending and (c) bifurcation keys for 72 PUFs. d,e) LZ entropy distributions obtained from bit streams of the (d) ending and (e) bifurcation keys. f,g) Normalized Intra-HD and Inter-HD histograms with Gaussian fittings for (f) ending and (g) bifurcation keys. Insets in (f) and (g) show magnified Intra-HD distributions.

in Figure S7 (Supporting Information), the fingerprint pattern image is converted into a skeleton image through image processing. Ending and bifurcation points are extracted from this, generating 2D binary codes of 30 × 90 bits for endings and 20 × 60 bits for bifurcations (Figure 3a). The randomness of a fingerprint optical PUF can be assessed by bit uniformity. It quantifies the degree to which the output bits of the generated PUF are uniformly distributed between 0 and 1, with an ideal PUF exhibiting a bit uniformity of 0.5. Bit uniformity histograms are obtained for 72 ending and bifurcation PUFs, and Gaussian fittings are applied to determine the mean and standard deviation. The bit uniformities for endings and bifurcations are 0.5005 ± 0.0545 and 0.5281 ± 0.0673, respectively, demonstrating that the obtained fingerprint patterns exhibit randomness (Figure 3b,c). To further evaluate the randomness and complexity, informational entropy (Shannon entropy) and Lempel–Ziv entropy (LZ entropy) are calculated. Informational entropy describes how bits are randomly distributed within a binary sequence, with values closer to 1 indicating greater randomness. The distributions of bits along the rows and columns of the 2D binary codes for endings and bifurcations are plotted (Figure S8, Supporting Information), and informational entropy heatmaps are obtained for all 72 optical PUFs (Figure S9, Supporting Information). LZ entropy analyzes repetitive patterns within the PUF output bitstream to assess its compressibility, and it can overcome the drawbacks of informational entropy, which cannot consider the periodicity of the binary sequences in the bit streams. LZ entropy ranges from 0 to 1, with values closer to 1 indicating greater complexity and randomness. The average LZ entropies of the binary sequences for the ending and bifurcation are 0.8644 ± 0.0300 and 0.9374 ± 0.0376, respectively (Figure 3d,e). The resulting average values (≈90% of the ideal value) of the informational and LZ entropy show that the optical fingerprint PUFs are random and exhibit an appropriate level of complexity. Next, to validate the distinguishability between outputs of different PUF codes, we examine uniqueness, which can be assessed by the Inter-Hamming distance (Inter-HD). The Hamming distance is the number of different bits between two binary sequences. Ideally, the normalized Inter-HD converges to 0.5. Histograms and Gaussian fittings of the normalized Inter-HD are obtained from ${}_{72}C_{71}$ (=2556) comparisons for each binary sequence (Figure 3f,g). The means and standard deviations of the Inter-HD for the ending and

bifurcation are 0.4986 ± 0.0141 and 0.4967 ± 0.0201, respectively. The effective encoding capacity (EC), which represents the number of unique outputs that PUF can generate, is evaluated for binary bits with an EC = $2^{\mu(1-\mu)/\sigma^2}$, where μ and σ are mean and standard deviation values of Inter-HD.[7] The EC = $2^{1\,257}$ ($\approx 10^{378}$) and 2^{618} ($\approx 10^{186}$) for endings and bifurcations, respectively. For a PUF to be practically used, it should exhibit reproducibility, which refers to the ability to observe the same response from the same PUF, and thus the Intra-Hamming distance (Intra-HD) is calculated. Similar to the Inter-HD calculation, the histogram of the normalized Intra-HD with Gaussian fit is derived from repeated measurements of 72 identical PUFs (Figure 3f,g). Means and standard deviations of the Intra-HD for the ending and bifurcation are 0.2123 ± 0.0746 and 0.1613 ± 0.0554, respectively. Using Intra-HD and Inter-HD, we examined two error rates, a false positive rate (FPR) and a false negative rate (FNR), to quantify the precision of the authentication process. The probability that a fake PUF is identified as authentic (Type-I error) is known as the FPR, and an authentic PUF is identified as fake (Type-II error) is known as the FNR. The FPR and FNR determined by the threshold are calculated based on the overlapping area of the Gaussian distributions of Inter-HD and Intra-HD reported in Figure 3f,g. We obtained a threshold value of 0.4474, FPR = 1.342×10^{-4}, and FNR = 8.078×10^{-4} for ending, and the threshold value of 0.4042, FPR = 1.995×10^{-6}, and FNR = 5.769×10^{-6} for bifurcation.

From users' perspective, practical authentication of PUFs requires additional consideration of changes in image conditions such as shift and rotation. We correct the shift and rotation of the image generated from the user image by comparing it with the database using the feature matching algorithm (Scale-Invariant Feature Transform, SIFT) and confirmed that the optical binary code obtained from the user image is authentic (Figure S10, Supporting Information). Since SIFT algorithm extracts features that are robust to the scale and rotation of the image, it always extracts features that are extracted from the same location even if the size of the image changes or is rotated.[71] In the database image, 6130 key points were detected. For an image taken at different angle and shift, 392 key points were successfully matched with the database image, and the same area as the database image is extracted based on the matching points. After obtaining binary codes for ending and bifurcation, HDs between the database and user image are 0.2733 < 0.4474 (threshold) for ending and 0.2183 < 0.4042 (threshold) for bifurcation, indicating that user image is authentic. SIFT algorithm between the database image and fake image shows that only two key points out of 6130 key points are matched (Figure S11, Supporting Information).

2.4. Statistical Evaluation of the Performance for Electrical PUF

We obtained the transfer curves from the 4 × 6 array of OFET devices in the PUF (**Figure 4**). Due to the p-type semiconductor characteristics of 2FPh-BTBT-C8, attributed to its BTBT core,[72,73] the transfer curves are measured with a source-drain voltage of −50 V and a gate voltage ranging from 10 to −50 V. The results of repeated measurements of transfer curves show that each OFET device exhibits reproducible and independent electrical signals (Figure S12, Supporting Information). Electrical characteristics for each device, such as threshold voltage (V_{th}), hole mobility (μ) in the saturation regime (V_{SD} = −50 V), on-current at V_G = −50 V (I_{DS}), and subthreshold slope (S-slope), are extracted (Figure 4a). These characteristics are mapped onto a 4 × 6 2D matrix, and using the median value as a threshold, four 4 × 6 binary codes per sample are generated (Figure 4b-i). To assess the performance of the electrical PUFs, bit uniformity, LZ entropy, Intra-HD, and Inter-HD are calculated using the same statistical analyses as for the optical PUFs, based on a total of 15 PUF samples. Bit uniformities are measured as 0.5 for all characteristics except for V_{th}, in which identical values cause deviations from 0.5 in bit uniformity (Figure S13a–d, Supporting Information). LZ entropy values are obtained as 1 for all data points except one in the mobility characteristic (Figure S13e–h, Supporting Information). The results of bit uniformity and LZ entropy demonstrate that the electrical PUF satisfies the randomness property. Histograms of Inter-HD and Intra-HD with Gaussian fittings for each characteristic are shown in Figure 4j–m. Based on the Gaussian fittings, means and standard deviations of the Intra-HD for the V_{th}, μ, I_{DS}, and S-slope are 0.0806 ± 0.0833, 0.0083 ± 0.0234, 0.0139 ± 0.0302, and 0.0028 ± 0.0108, respectively. Means and standard deviations of the Inter-HD for the V_{th}, μ, I_{DS}, and S-slope are 0.5016 ± 0.1051, 0.4563 ± 0.1109, 0.4786 ± 0.1103, and 0.4952 ± 0.1039, respectively. To evaluate the precision of the authentication, threshold values, FPRs, and FNRs are calculated for all electrical characteristics. For V_{th}, threshold = 0.2766, FPR = 1.618×10^{-2}, and FNR = 1.322×10^{-2}. For μ, threshold = 0.0949, FPR = 5.588×10^{-4}, and FNR = 1.051×10^{-4}. For I_{DS}, threshold = 0.1227, FPR = 6.235×10^{-4}, and FNR = 1.547×10^{-4}. For S-slope, threshold = 0.0539, FPR = 1.079×10^{-5}, and FNR = 1.008×10^{-6}. In addition to the electrical parameters we have presented, extracting parameters such as charge mobility and current at different voltages can increase the number of response factors of electrical PUFs, which can be used for hierarchical authentication.

2.5. Reconfigurability of the PUF

Whereas PUFs with a determined structure after fabrication generate fixed responses based on a static physical structure, reconfigurable PUFs allow for the transformation of responses by modifying initial states or structures. Consequently, reconfigurable PUFs can generate multiple unique PUF responses from a single device. This flexibility enables it to counter various attacks, generate adaptable keys, and support multi-factor authentication. Our PUF is composed of a thermotropic LC, 2FPh-BTBT-C8, so reconfigurability can be realized through changes in optical texture based on thermal phase transition (Video S2, Supporting Information). When the fabricated 2FPh-BTBT-C8 film is heated to the Iso phase and subsequently cooled, the original fingerprint pattern is erased, and a new one emerges, generating a new 2D binary key by image processing (**Figure 5**a,b). To ensure that randomness is retained across heating and cooling cycles, we calculate the bit uniformity of the optical PUFs. For ending and bifurcation, the means and standard deviations are 0.4882 ± 0.0344 and 0.4873 ± 0.0378, respectively. It indicates that the PUFs maintain randomness even after heating and cooling processes (Figure 5c,e). Furthermore, 2D correlations are investigated to evaluate the uniqueness of optical

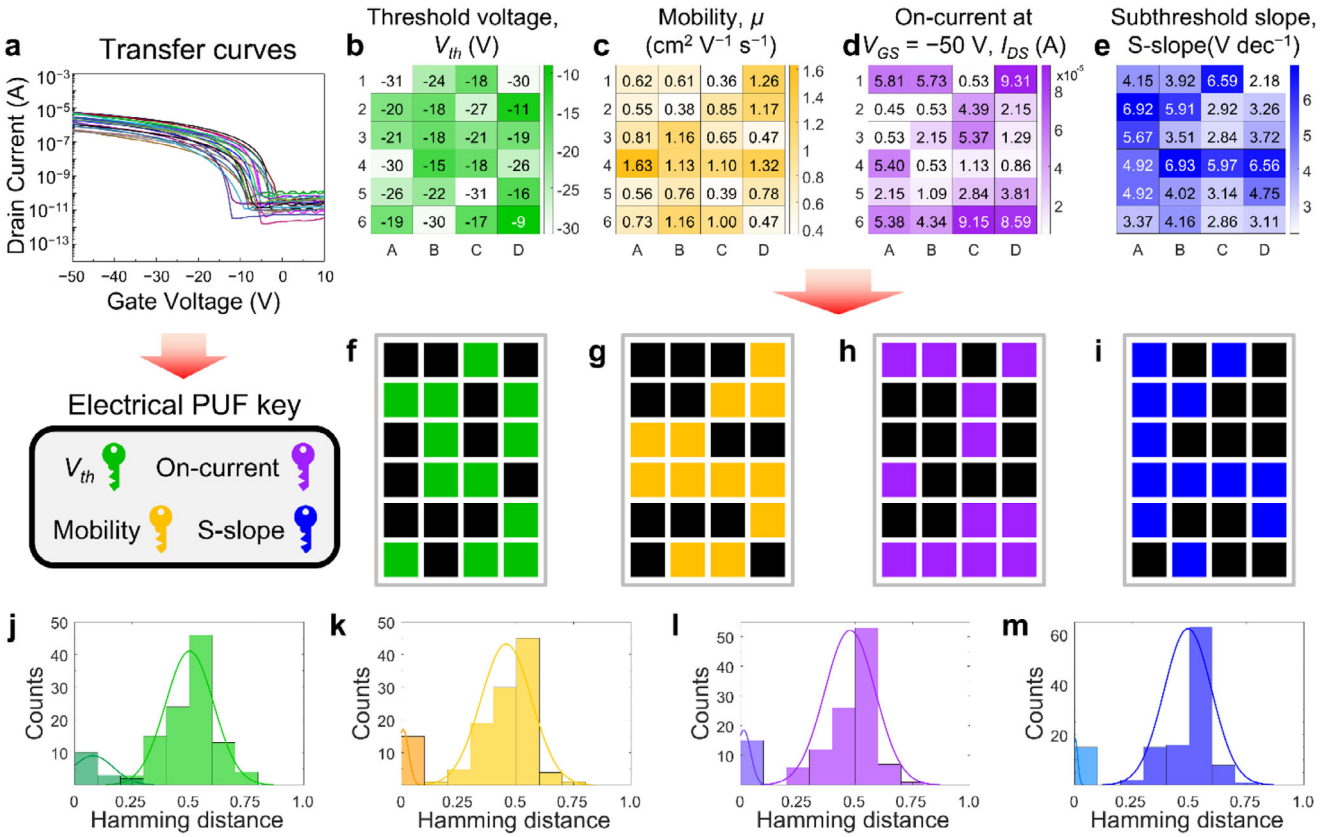

Figure 4. Electrical 2D binary PUF keys and evaluation of PUF performance by statistical analysis. a) Transfer curves of 24 devices in one OFET sample for generating electrical PUF keys using various electrical characteristic parameters. b–e) Heatmap of 24 devices (6 × 4 array) for each electrical characteristic, (b) V_{th}, (c) μ, (d) I_{DS}, and (e) S-slope. f–i) Binary key for each electrical characteristic obtained by determining the threshold value as median value. Note that threshold value for each characteristic is set as median value. j–m) Normalized Intra-HD and Inter-HD histogram with a Gaussian fit for each electrical characteristic obtained by 15 PUFs.

PUFs across heating and cooling cycles within a single PUF. Means and standard deviations of the similarity indices across distinct cycles are 0.5009 ± 0.0115 for ending and 0.5033 ± 0.0172 for bifurcation, indicating minimal correlation between reconfigured optical PUFs across heating and cooling cycles (Figure 5d,f).

For the electrical PUF, it is confirmed that heating and cooling process leads to a different transfer curve distribution due to changes in the orientation of 2FPh-BTBT-C8, generating new electrical characteristic keys (Figure 5g,h). Bit uniformity across heating and cooling cycles shows minimal deviation from the ideal value of 0.5 (Figure 5i), and the similarity index for 2D correlation of the mobility characteristic is 0.55 ± 0.08 (Figure 5j). Note that only the mobility characteristic is shown in Figure 5 as a representative example of the reconfigurability of the electrical PUF, and the statistical analysis results for all electrical characteristics are presented in Figures S14 and S15 (Supporting Information). The reason why the mean value of the similarity index of the electrical PUF is farther from the ideal value of 0.5 and the standard deviation is larger than that of the optical PUF is that the length of the binary sequence is shorter than that of the optical PUF so that the statistical value changes significantly even with a small pixel change. The results from bit uniformity and the similarity index based on Inter-HD calculations demonstrate that 2FPh-BTBT-C8 can reconfigure into entirely new and random structures without memory effect.

2.6. Multidimensional Authentication and Improvement of Security of the PUF

Our PUF enables multidimensional authentication by utilizing optical and electrical challenges while providing multi-factor responses for each challenge (**Figure 6**a). The multidimensional authentication process is achieved through a hierarchical verification approach. Once the types of challenges and responses (e.g., ending, bifurcation, V_{th}, etc.) to be used for authenticating an unknown PUF are specified, the unknown PUF is compared to the database of PUF for each type, and a similarity index is calculated. If even one type fails to exceed the threshold, the PUF is classified as fake, providing enhanced security compared to a single PUF system. The multidimensional feature, which combines optical and electrical PUFs, offers flexibility in selecting the preferred challenge–optical or electrical–based on the application's requirements. Users can choose either one or use them together based on their circumstances, allowing flexible authentication. Additionally, due to the liquid crystalline properties of 2FPh-BTBT-C8, irreversible reconfiguration can be achieved through

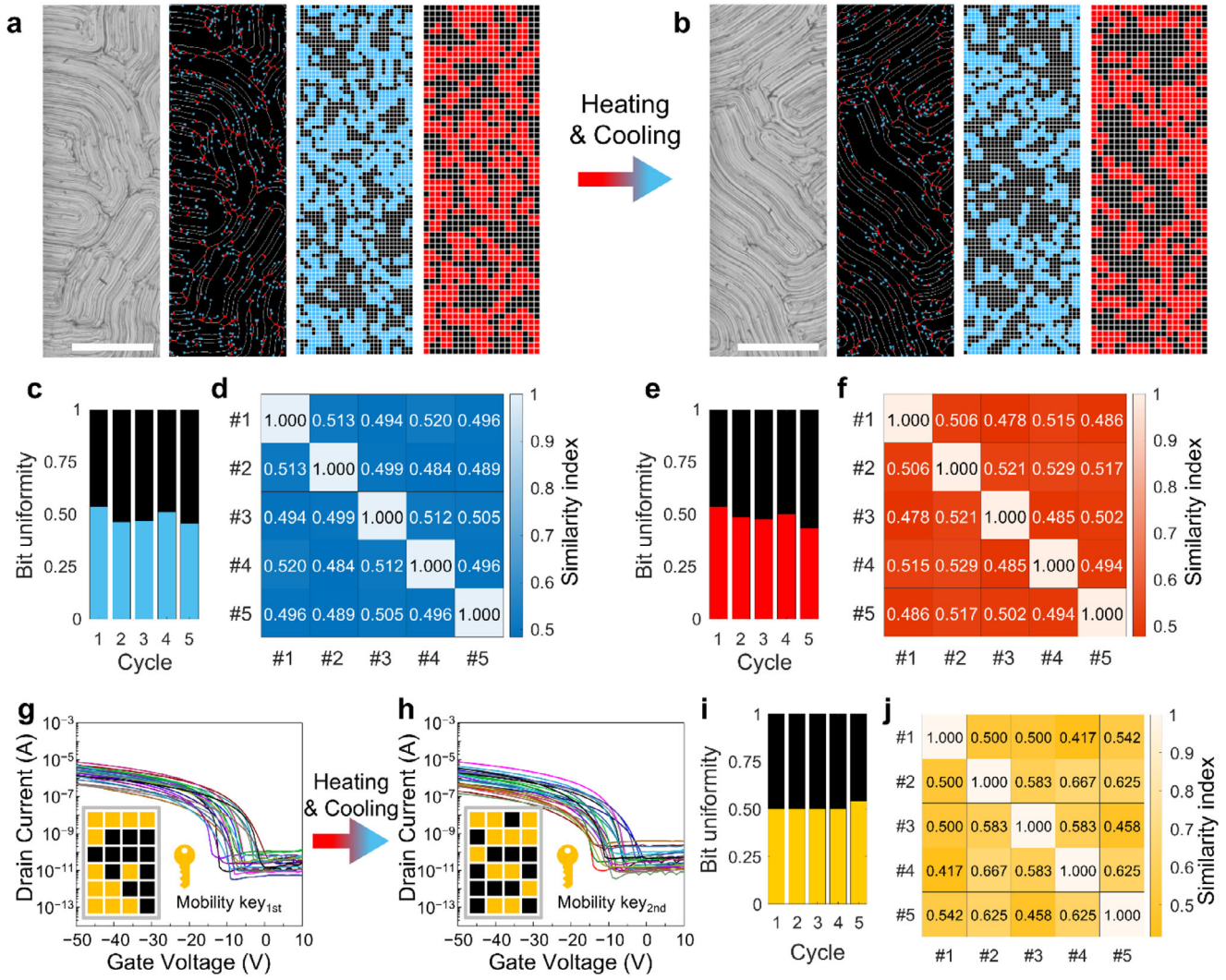

Figure 5. Reconfigurability test of the PUF. a,b) Optical image, fingerprint pattern, ending key, and bifurcation key (a) before and (b) after the heating and cooling process. All images and keys are irreversibly changed after heating to Iso phase and then cooling to the room temperature. Scale bars, 100 µm. c,e) Bit uniformity plots and d,f) 2D correlations of (c,d) ending and (e,f) bifurcation keys for 5 heating and cooling cycles. g,h) Transfer curves and generated mobility key (g) before and (h) after the heating and cooling process. Only the mobility key is shown here as a representative electrical characteristic of OFET. i) Bit uniformity plot and j) 2D correlation of mobility keys for reconfigurability test with 5 heating and cooling processes.

heating to the Iso phase temperature and subsequent cooling, ensuring recovery from external attacks or generating new keys when needed by users. In fact, reconfiguration interrupts synchronization with the database, which imposes limitations on the authentication in a practical usage environment. Nevertheless, since the PUFs remain embedded within the device, their encryption capabilities remain intact. Therefore, data can be securely protected through encryption after reconfiguration and subsequently re-enrolled in the database when needed. In contrast, PUFs without reconfigurability usually need to be physically replaced when the key is exposed. It might be difficult or impossible to replace the PUF if it is incorporated into a sensitive or crucial component of the application. In this context, reconfigurability enables a practical method of restoring authentication by allowing database re-enrollment without the need for hardware substitution.

The 2FPh-BTBT-C8 film exhibits birefringence due to its molecular anisotropy, allowing POM images to be converted into octal 2D color codes to generate additional optical PUFs (Figure 6b). Under the crossed polarizer state, the optical phase difference between ordinary and extraordinary polarization is related to the birefringence color according to the wavelength and intensity of the transmitted light. Differences in molecular orientation and microstructures maximize variations in birefringence colors and create highly complex color codes at the microscale, derived from the Michel-Lévy birefringence chart.[74] Furthermore, the additional phase retardation plate ($\lambda = 530$ nm) generates yellowish and blueish domains when the slow axis of the positive birefringent 2FPh-BTBT-C8 molecule is parallel or perpendicular to the slow axis of the λ plate, respectively. This also creates random color codes different from under the cross polarizers due to the retardation differences. For extracting

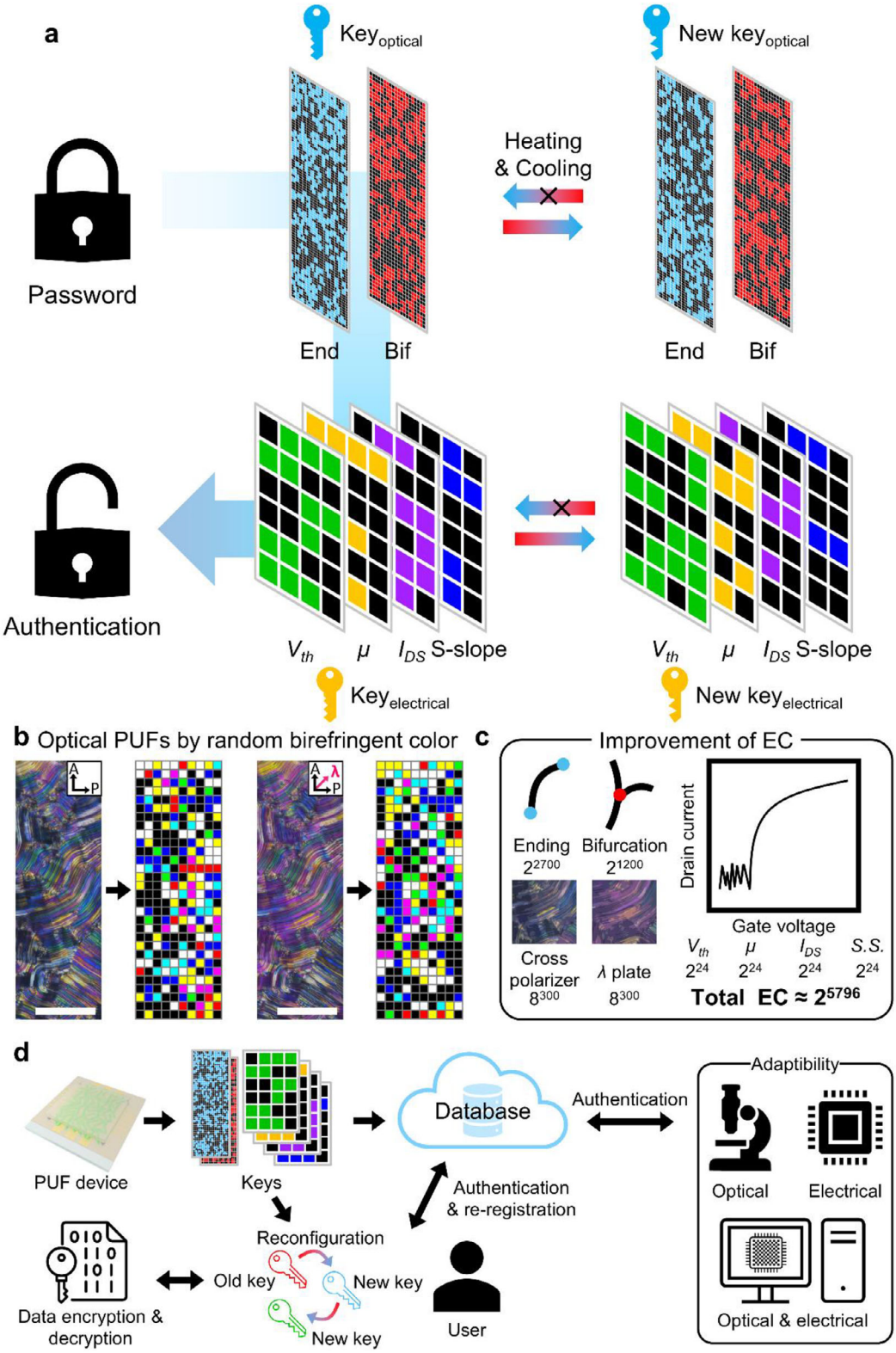

Figure 6. Multidimensional authentication and improvement of encoding capacity. a) Multidimensional authentication scheme generated with optical and electrical PUFs. The LC phase of 2FPh-BTTB-C8 provides reconfigurable ability to induce unpredictable responses, enhancing security and dynamic adaptability. b) Possibility of generation of additional optical PUFs using birefringent colors under the cross polarizers and retardation plate. Scale bars, 100 µm. c) Improvement of EC by integrating additional optical and electrical PUFs. d) Application scheme of PUFs in anticounterfeiting system, including reconfigurability and adaptability.

octal code, birefringent image is separated to red, green, and blue channel, followed by binning and binarizing processes for each channel (Figure S16, Supporting Information). Octal codes are then obtained by combining the binary codes. As shown in the schematic illustration in Figure S17 (Supporting Information), authentication can be realized by converting the octal code into three binary codes of red, green, and blue and performing hierarchical verification for each code. Figure 6c demonstrates the potential to improve EC by integrating various optical and electrical PUFs. While the ideal total EC using all proposed PUF types is $\approx 2^{5\,796} \approx 10^{1\,700}$, further enhancements are achievable by increasing the pixel count in the 2D codes of optical PUFs, utilizing the angle variation between the phase retardation plate and the polarizer as multi-challenges, or incorporating electrical characteristics at specific gate or source-drain voltages. These strategies could enable the realization of higher ECs and the application of the system as a strong PUF.

We propose application scenarios for LC-based PUFs focusing on their multidimensionality and reconfigurability, as illustrated in Figure 6d. In the reconfiguration scenario, the PUF can be reconfigured by the user and utilized for data encryption and decryption when a new key is required during usage. The new key can then be re-registered to the database to reactivate authentication. In the multidimensional scenario, the dual capability of generating both optical and electrical responses enables users to select their preferred authentication method, offering adaptability to various application environments.

2.7. Stability of the PUF

Since PUFs should generate consistent and reliable responses under diverse environmental conditions, their stability is essential for practical applications. As shown in Figure S4b (Supporting Information), the PUF device is positioned between two glass substrates, and the material remains in a crystalline state, ensuring mechanical stability unless physically damaged. Although the requirement for the material to exist in a thin film between glass substrates acts as a restricted condition, this structure provides notable resistance to mechanical stress. To assess the device's environmental robustness, we conducted a series of tests. First, a long-term stability test is carried out to evaluate durability over time (Figures S18 and S19, Supporting Information). The device maintains its original fingerprint textures after seven days, indicating that the LC material retains a stable crystalline structure at room temperature. We also examined thermal stability considering the situation in which heat is generated depending on the use of the application when PUF devices are embedded in (Figures S20 and S21, Supporting Information). After heating the LC material to 100 °C for 30 min and subsequently cooling it to 30 °C, no changes are observed in the optical fingerprints. This demonstrates that the material preserves its macroscopic crystalline phase even after prolonged high-temperature exposure. Humidity tests are further performed to reflect real-world usage scenarios (Figures S22 and S23, Supporting Information). Comparison of optical textures at relative humidity (RH) 30% and RH 70% shows no noticeable difference, indicating that moisture has negligible impact. This is attributed to the hydrophobic molecular structure of the LC material, composed of fluorinated, aromatic, and alkyl groups, and its encapsulation within the glass cell. Although condensation of water vapor on the optics or sample surface at RH 70% causes optical haze under our experimental conditions, HD of optical binary keys between RH 30% and RH 70% is within the average ± standard deviation range of inter-HD (Figure S22, Supporting Information). Moisture effect can be prevented by applying hydrophobic coatings or increasing the surface temperature above the dew point at high humidity. For each condition, HDs between initial and after-test binary codes of optical and electrical PUFs are calculated to evaluate authentication (Figures S18–S23, Supporting Information). All HD values, except for HD between RH 30% and RH 30% from RH 70% for S-slope binary key, remain below the predetermined threshold, confirming that the device maintains reliable authentication capability even under varied environmental stress. For HD between RH 30% and RH 30% from RH 70% for S-slope binary key, HD exceeded the threshold due to only one bit value (Figure S23, Supporting Information). To evaluate the reconfiguration cycles, we monitored the changes in optical fingerprint textures under repeated thermal cycles consisting of heating to the isotropic phase and subsequent cooling to 30 °C (Figure S24, Supporting Information). Throughout ten cycles, distinct and stable fingerprints are consistently generated, demonstrating complete reconfiguration without any damage or deformation to the LC materials and PUF device.

3. Conclusion

Reconfigurable and multidimensional PUFs are fabricated using an LC-based OFET device. The random nucleation and growth during thermal phase transition plays a pivotal role in unpredictable fingerprint patterns as well as electrical signals for the combined optical and electrical PUFs. Statistical analysis confirms randomness and uniqueness, exhibiting encoding capacity as high as $10^{1\,700}$ combining a total of 8 different codes. Notably, the LC nature of the present OSC material introduces reconfigurability, addressing the limitations of PUFs with fixed structures, and multidimensional authentication can be achieved through hierarchical verification due to the multi-response factors. Overall, we anticipate that the multidimensionality, dynamic adaptability, and expandability of our PUF can be applied in various fields requiring on-demand security system, such as IoT, secure authentication, and anticounterfeiting.

4. Experimental Section

Materials and Fabrication of the PUF Devices: 2FPh-BTBT-C8 was synthesized by modifying a synthetic scheme in the previous study (Figure S1, Supporting Information).[52] Differential scanning calorimetry (DSC) curve of the 2FPh-BTBT-C8 was obtained by TA instruments DSC 25 at heating and cooling rates of 5 °C min^{-1}. To fabricate the OFET devices, ITO-coated glass substrates (2.5 × 2.5 cm^2) were chemically washed with acetone, ethanol, and deionized water. Planar anchoring polyimide (PAPI; DL-2193, Shenzhen Dalton Electronic Materials Co., LTD) was spin-coated on the ITO-coated substrate to induce degenerate planar alignment of LC molecules and to use PAPI film as a dielectric layer. PAPI-coated substrates were pre-baked on the hot plate at 60 °C for 5 min and then hard-baked at 200 °C for 2 h. Au (40 nm)/Ti (5 nm) electrodes for source and drain were deposited on the substrates by a thermal evaporator with a metal

shadow mask. To induce low contact resistance, pentafluorobenzenethiol (PFBT, Sigma–Aldrich) in ethanol solution (0.1 wt.%) was spin-coated on the substrate to fabricate self-assembled monolayers (SAMs), followed by thermal annealing at 120 °C for 1 h. Finally, the substrate was sandwiched with a top PAPI-coated glass substrate using 4 µm diameter silica particle and UV-curable with heat-resistible adhesive to achieve a uniform cell gap. The 2FPh-BTBT-C8 powder was loaded at the sandwich cell's entrance and injected into the cell by capillarity at its Iso phase (≈212 °C). Except for the analysis according to the cooling rate in Figure 2, the samples were cooled to the Cr phase at a rate of 5 °C min^{-1}.

Optical Characterization: The optical textures of the 2FPh-BTBT-C8 film in the sandwich cell were observed by a polarized optical microscope (Nikon Eclipse LV100POL and Nikon Eclipse Ti2), and images were taken by a charge-coupled device camera (Nikon DS-Ri1 for LV100POL and Nikon DS-Ri2 for Ti2).

Molecular Structural Characterization Using Grazing Incidence X-Ray Diffraction (GIXD): GIXD experiments were conducted at the 9A U-SAXS and 6D C&S UNIST-PAL beamlines in the Pohang Accelerator Laboratory (PAL). The X-ray energy was 11.08 keV for the GIWAXD experiment and 18.986 keV for the PXRD measurement for profile matching, respectively. The sample-to-detector distance (SDD) was 222.10 mm for the GIWAXD experiment and 301.40 mm for the PXRD measurement. The X-ray diffractograms were recorded with a 2D CCD camera (Rayonix SX165).

Electrical Characterization: The transfer and output characteristics of the bottom-gate bottom-contact OFET devices were measured by an electrical parameter analyzer (Keithley 4200A-SCS) in a N_2-filled glovebox. The charge carrier mobility (μ) was calculated at the saturation region in the transfer curves using the following equation:

$$I_{DS} = (WC_i/2L)\,\mu(V_G - V_{th})^2 \tag{1}$$

where W is the width (500 µm) of the source and drain channel, and L is the length (200 µm) between the source and drain. C_i is the capacitance per unit area of the gate insulator (≈76.5 pF mm^{-2}).[54] V_{th} is the threshold voltage extracted from extrapolating a linear fitting of $-\sqrt{I_{DS}}$ versus V_{GS}.

Statistical Evaluation of PUF Performance: Bit uniformity: Bit uniformity, the distribution of 1- or 0-bits in the bit streams, can be calculated by following equation.

$$Bituniformity = \frac{1}{N}\sum_{k=1}^{N} s_k \tag{2}$$

where s_k is k-th bit, which values are 0 or 1, and N is the number of bits in the single binary sequence. N is 2700 for ending (30 × 90), 1200 for bifurcation (20 × 60), and 24 for electrical PUF keys, respectively. Ideally, bit uniformity is 0.5.

Informational Entropy (Shannon entropy): The randomness of PUF was characterized by the Shannon entropy (E) for each row or column of each PUF. Shannon entropy can be calculated as follows.

$$E_\alpha = -\left[p_\alpha \log_2 p_\alpha + (1-p_\alpha)\log_2(1-p_\alpha)\right] \tag{3}$$

where α is either the x- (row) or y-axis (column) of the array, and p_α is bit uniformity along the x or y axes. Ideally, Shannon entropy is 1 for $p_\alpha = 0.5$.

Lempel–Ziv (LZ) Entropy: LZ entropy can overcome the limitations of ordinary informational entropy, which cannot consider the periodicity of the binary sequences in the bit streams. LZ entropy can be calculated by combining bit uniformity and LZ complexity, which represents the amount of unique binary sequence combinations.[75] The LZ complexity (C_{LZ}) is calculated by an existing open-source algorithm. LZ entropy (S_{LZ}) is calculated as below.

$$S_{LZ} = \frac{-C_{LZ}\log_2 N\left(p\log_2 p + (1-p)\log_2(1-p)\right)}{N} \tag{4}$$

where p is bit uniformity of the binary sequence, and N is the number of bits in the single binary sequence.

Hamming Distance (HD): HD between two binary sequences represents the number of different bits in the same position of the bit streams. Intra-HD and Inter-HD were calculated to evaluate whether the same PUFs were considered the same and different PUFs are distinguished from each other. Normalized HD was calculated as follows.

$$NormalizedHammingdistance\quad (HD) = \frac{\sum_{k=1}^{N}\left(s_{i,k} \oplus s_{j,k}\right)}{N} \tag{5}$$

where $s_{i,k}$ is k-th bit of the i-th binary sequence. $i = j$ for Intra-HD, and $i \neq j$ for Inter-HD. $\oplus$ symbol indicates XOR operator. N is the number of bits in the single binary sequence. Ideally, Intra-HD should be closer to 0, which means the two PUFs are the same, and Inter-HD has to be closer to 0.5, which shows the two PUFs are distinct. For optical PUF, the histograms with Gaussian fit were obtained with 72 binary sequences for ending and bifurcation, respectively. The distributions for intra-HD and inter-HD consist of 72 and $_{72}C_2$ (= 2556) data points, respectively. For electrical PUF, the histograms with Gaussian fit for intra-HD and inter-HD were obtained with 15 binary sequences, which consisted of 15 and $_{15}C_2$ (= 105) data points.

The following equation simply expresses the similarity index for the reconfigurability test.

$$Similarity\ \ index = 1 - Normalized\ \ HD \tag{6}$$

Supporting Information

Supporting Information is available from the Wiley Online Library or from the author.

Acknowledgements

This project was supported by a grant from the National Research Foundation in Korea (RS-2023-00273025 and 2021M3H4A3A01050378). [Correction added on June 24, 2025, after first online publication: The copyright line was changed.]

Conflict of Interest

The authors declare no conflict of interest.

Author Contributions

H.S.Y. performed conceptualization, formal analysis, investigation, software, validation, visualization, wrote the original draft, and wrote, reviewed, and edited the draft. D.W. and D.M.W. provided resources. S.Y. performed formal analysis and investigation. G.P. performed software. M.S.K. performed wrote, reviewed, and edited the draft. T.J.S. performed formal analysis and investigation. M.J.H. performed conceptualization, formal analysis, investigation, wrote, reviewed, and edited the draft, and supervision. D.K.Y. performed conceptualization, wrote, reviewed, and edited the draft., supervision, and funding acquisition.

Data Availability Statement

The data that support the findings of this study are available from the corresponding author upon reasonable request.

Keywords

liquid crystals, multidimensional PUF, organic field-effect transistors, physical unclonable functions, reconfigurability

Received: March 3, 2025
Revised: May 19, 2025
Published online:

[1] A. Banafa, *Secure and Smart Internet of Things (IoT): Using Blockchain and AI*, River Publishers, Aalborg, Nordjylland, Denmark **2018**, pp i–xx.
[2] H. Lasi, P. Fettke, H.-G. Kemper, T. Feld, M. Hoffmann, *Bus. Inf. Syst. Eng.* **2014**, *6*, 239.
[3] S. Kumar, P. Tiwari, M. Zymbler, *J. Big Data* **2019**, *6*, 111.
[4] M. Dowd, J. McDonald, J. Schuh, *The Art of Software Security Assessment: Identifying and Preventing Software Vulnerabilities*, Pearson Education, London, UK **2006**.
[5] A. Shukla, B. Katt, L. O. Nweke, P. K. Yeng, G. K. Weldehawaryat, *Comput. Sci. Rev.* **2022**, *45*, 100496.
[6] G. McGraw, *IEEE Secur. Priv.* **2004**, *2*, 80.
[7] R. Pappu, B. Recht, J. Taylor, N. Gershenfeld, *Science* **2002**, *297*, 2026.
[8] C. Herder, M.-D. Yu, F. Koushanfar, S. Devadas, *Proc. IEEE* **2014**, *102*, 1126.
[9] R. Arppe, T. J. Sørensen, *Nat. Rev. Chem.* **2017**, *1*, 31.
[10] Y. Gao, S. F. Al-Sarawi, D. Abbott, *Nat. Electron.* **2020**, *3*, 81.
[11] H. Ning, F. Farha, A. Ullah, L. Mao, *IET Circuits, Devices Syst.* **2020**, *14*, 407.
[12] R. Maes, I. Verbauwhede, in *Physically Unclonable Functions: A Study on the State of the Art and Future Research Directions BT – Towards Hardware-Intrinsic Security: Foundations and Practice*, (Eds: A.-R. Sadeghi, D. Naccache), Springer, Berlin Heidelberg **2010**, pp 3–37.
[13] T. McGrath, I. E. Bagci, Z. M. Wang, U. Roedig, R. J. Young A PUF Taxonomy, *Appl. Phys. Rev.* **2019**, *6*, 11303.
[14] T. Zhang, L. Wang, J. Wang, Z. Wang, M. Gupta, X. Guo, Y. Zhu, Y. C. Yiu, T. K. C. Hui, Y. Zhou, C. Li, D. Lei, K. H. Li, X. Wang, Q. Wang, L. Shao, Z. Chu, *Nat. Commun.* **2023**, *14*, 2507.
[15] Y. Lu, H. Chen, H. Cheng, H. Qiu, C. Jiang, Y. Zheng, *ACS Appl. Nano Mater.* **2022**, *5*, 9298.
[16] K. Wang, W. Lai, D. Yang, X. Yu, *ACS Appl. Nano Mater.* **2024**, *7*, 25535.
[17] M. R. Carro-Temboury, R. Arppe, T. Vosch, T. J. Sørensen, *Sci. Adv.* **2018**, *4*, 1701384.
[18] Y. Gu, C. He, Y. Zhang, L. Lin, B. D. Thackray, J. Ye, *Nat. Commun.* **2020**, *11*, 516.
[19] A. F. Smith, P. Patton, S. E. Skrabalak, *Adv. Funct. Mater.* **2016**, *26*, 1315.
[20] Q. Li, F. Chen, J. Kang, J. Su, F. Huang, P. Wang, X. Yang, Y. Hou, *Adv. Funct. Mater.* **2021**, *31*, 2010537.
[21] Z. Wang, H. Wang, P. Wang, Y. Shao, *ACS Appl. Mater. Interfaces* **2024**, *16*, 27926.
[22] Z. C. Meijs, H. S. Yun, P. Fandre, G. Park, D. K. Yoon, L. Isa, *ACS Appl. Mater. Interfaces* **2023**, *15*, 53053.
[23] K. Wang, J. Shi, W. Lai, Q. He, J. Xu, Z. Ni, X. Liu, X. Pi, D. Yang, *Nat. Commun.* **2024**, *15*, 3203.
[24] J. W. Leem, M. S. Kim, S. H. Choi, S.-R. Kim, S.-W. Kim, Y. M. Song, R. J. Young, Y. L. Kim, *Nat. Commun.* **2020**, *11*, 328.
[25] M. S. Kim, G. J. Lee, J. W. Leem, S. Choi, Y. L. Kim, Y. M. Song, *Nat. Commun.* **2022**, *13*, 247.
[26] H. J. Bae, S. Bae, C. Park, S. Han, J. Kim, L. N. Kim, K. Kim, S.-H. Song, W. Park, S. Kwon, *Adv. Mater.* **2015**, *27*, 2083.
[27] D. N. Minh, L. A. T. Nguyen, Q. H. Nguyen, T. Van Vu, J. Choi, S. Eom, S. J. Kwon, Y. Kang, *Adv. Mater.* **2023**, *35*, 2208151.
[28] I. Murataj, C. Magosso, S. Carignano, M. Fretto, F. F Lupi, G. Milano, *Nat. Commun.* **2024**, *15*, 10576.
[29] M. Ma, Z. Jiang, T. Ma, X. Gao, J. Li, M. Liu, J. Yan, X. Jiang, *Adv. Funct. Mater.* **2024**, *34*, 2405239.
[30] J. H. Kim, S. Jeon, J. H. In, S. Nam, H. M. Jin, K. H. Han, G. G. Yang, H. J. Choi, K. M. Kim, J. Shin, S. W. Son, S. J. Kwon, B. H. Kim, S. O. Kim, *Nat. Electron.* **2022**, *5*, 433.
[31] B. H. Wu, C. Zhang, N. Zheng, L. W. Wu, Z. K. Xu, L. S. Wan, *ACS Appl. Polym. Mater.* **2019**, *1*, 47.
[32] G. Park, H. Park, J. M. Wolska, J. G. Park, D. K. Yoon, *Mater. Horiz.* **2022**, *9*, 2542.
[33] G. Park, Y.-S. Choi, S. J. Kwon, D. K. Yoon, *Adv. Mater.* **2023**, *35*, 2303077.
[34] S. Nocentini, U. Rührmair, M. Barni, D. S. Wiersma, F. Riboli, *Nat. Mater.* **2024**, *23*, 369.
[35] K. Kim, S.-U. Kim, M.-Y. Choi, M. H. Saeed, Y. Kim, J.-H. Na, *Light: Sci. Appl.* **2023**, *12*, 245.
[36] S. M. Park, G. Park, D. K. Yoon, *Adv. Mater.* **2023**, *35*, 2302135.
[37] Y. Wan, P. Wang, F. Huang, J. Yuan, D. Li, K. Chen, J. Kang, Q. Li, T. Zhang, S. Sun, Z. Qiu, Y. Yao, *J. Mater. Chem. C* **2021**, *9*, 13200.
[38] A. Wali, A. Dodda, Y. Wu, A. Pannone, L. K. Reddy Usthili, S. K. Ozdemir, I. T. Ozbolat, S. Das, *Commun. Phys.* **2019**, *2*, 39.
[39] H. Han, Y. J. Lee, J. Kyhm, J. S. Jeong, J.-H. Han, M. K. Yang, K. M. Lee, Y. Choi, T.-H. Yoon, H. Ju, S. Ahn, J. A. Lim, *Adv. Funct. Mater.* **2020**, *30*, 2006236.
[40] D. Kim, S. Im, D. Kim, H. Lee, C. Choi, J. H. Cho, H. Ju, J. A. Lim, *Adv. Funct. Mater.* **2023**, *33*, 2210367.
[41] R. Wang, K. Liang, S. Wang, Y. Cao, Y. Xin, Y. Peng, X. Ma, B. Zhu, H. Wang, Y. Hao, *Adv. Mater.* **2023**, *35*, 2210621.
[42] Y. Han, S. Lee, E. K. Lee, H. Yoo, B. C. Jang, *Adv. Sci.* **2024**, *11*, 2309221.
[43] K. M. Hwang, J. Y. Park, H. Bae, S. W. Lee, C. K. Kim, M. Seo, H. Im, D. H. Kim, S. Y. Kim, G. B. Lee, Y. K. Choi, *ACS Nano* **2017**, *11*, 12547.
[44] Z. Hu, J. M. M. L. Comeras, H. Park, J. Tang, A. Afzali, G. S. Tulevski, J. B. Hannon, M. Liehr, S. J. Han, *Nat. Nanotechnol.* **2016**, *11*, 559.
[45] U. Jung, C.-J. Beak, K. Kim, J.-H. Na, S.-H. Lee, *ACS Nano* **2024**, *18*, 27642.
[46] K. Kursawe, A.-R. Sadeghi, D. Schellekens, B. Skoric, P. Tuyls, in 2009 IEEE International Workshop on Hardware-Oriented Security and Trust, IEEE, Piscataway, NJ, USA **2009**, pp 22–29.
[47] Z. Gan, F. Chen, Q. Li, M. Li, J. Zhang, X. Lu, L. Tang, Z. Wang, Q. Shi, W. Zhang, W. Huang, *ACS Appl. Mater. Interfaces* **2022**, *14*, 5785.
[48] Y. Yang, R. Hui, X. Lu, L. Tang, Z. Gan, M. Li, J. Zhang, K. Chen, F. Chen, W. Huang, *ACS Photonics* **2024**, *11*, 4691.
[49] Y. Shao, N. Davila, F. Ebrahimi, J. A. Katine, G. Finocchio, P. K Amiri, *Adv. Electron. Mater.* **2023**, *9*, 2300195.
[50] A. Dodda, S. Subbulakshmi Radhakrishnan, T. F. Schranghamer, D. Buzzell, P. Sengupta, S. Das, *Nat. Electron.* **2021**, *4*, 364.
[51] Y. Kim, J. Lim, J. H. Lim, E. Hwang, H. Lee, M. Kim, I. Ha, H. Cho, J. Kwon, J. Oh, S. H. Ko, H. Pan, S. Hong, *Adv. Mater.* **2023**, *35*, 2212294.
[52] M. J. Han, D. Wei, Y. H. Kim, H. Ahn, T. J. Shin, N. A. Clark, D. M. Walba, D. K. Yoon, *ACS Cent. Sci.* **2018**, *4*, 1495.
[53] H. Iino, T. Usui, J. Hanna, *Nat. Commun.* **2015**, *6*, 6828.
[54] M. J. Han, D. Wei, H. S. Yun, S. Lee, H. Ahn, D. M. Walba, T. J. Shin, D. K. Yoon, *NPG Asia Mater* **2022**, *14*, 28.
[55] W. Kim, D. S. Kim, D. K. Yoon, *Giant* **2024**, *19*, 100324.
[56] S. Fratini, M. Nikolka, A. Salleo, G. Schweicher, H. Sirringhaus, *Nat. Mater.* **2020**, *19*, 491.
[57] M. P. M. Schelling, T. W. J. Verouden, T. C. M. Stevens, J.-M. Meijer, *Soft Matter* **2024**, *20*, 6343.
[58] L. Li, M. Salamończyk, S. Shadpour, C. Zhu, A. Jákli, T. Hegmann, *Nat. Commun.* **2018**, *9*, 714.
[59] A. Altomare, C. Cuocci, C. Giacovazzo, A. Moliterni, R. Rizzi, N. Corriero, A. Falcicchio, *J. Appl. Crystallogr.* **2013**, *46*, 1231.
[60] J. Rodríguez-Carvajal, *Phys. B Condens. Matter* **1993**, *192*, 55.
[61] X. Liu, T. Jin, H. Li, S. Wang, Z. Shen, J. Li, R. Chen, Y. Chen, Y. Han, *Macromolecules* **2024**, *57*, 4141.
[62] S. Park, M. H. Lee, K. S. Ahn, H. H. Choi, J. Shin, J. Xu, J. Mei, K. Cho, Z. Bao, D. R. Lee, M. S. Kang, D. H. Kim, *Adv. Funct. Mater.* **2016**, *26*, 4627.

[63] W. Deng, H. Lei, X. Zhang, F. Sheng, J. Shi, X. Zhang, X. Liu, S. Grigorian, X. Zhang, J. Jie, *Adv. Mater.* **2022**, *34*, 2109818.
[64] V. C. Sundar, J. Zaumseil, V. Podzorov, E. Menard, R. L. Willett, T. Someya, M. E. Gershenson, J. A. Rogers, *Science* **2004**, *303*, 1644.
[65] A. Y. B. Meneau, Y. Olivier, T. Backlund, M. James, D. W. Breiby, J. W. Andreasen, H. Sirringhaus, *Adv. Funct. Mater.* **2016**, *26*, 2326.
[66] I. Vladimirov, M. Kühn, T. Geßner, F. May, R. T. Weitz, *Sci. Rep.* **2018**, *8*, 14868.
[67] C. Liu, Y. Xu, Y.-Y. Noh, *Mater. Today* **2015**, *18*, 79.
[68] M. Kano, T. Minari, K. Tsukagoshi, *Appl. Phys. Lett.* **2009**, *94*, 143304.
[69] T. He, Y. Wu, G. D'Avino, E. Schmidt, M. Stolte, J. Cornil, D. Beljonne, P. P. Ruden, F. Würthner, C. D. Frisbie, *Nat. Commun.* **2018**, *9*, 2141.
[70] M. F. Calhoun, C. Hsieh, V. Podzorov, *Phys. Rev. Lett.* **2007**, *98*, 96402.
[71] D. G. Lowe, *Int. J. Comput. Vis.* **2004**, *60*, 91.
[72] H. Ebata, T. Izawa, E. Miyazaki, K. Takimiya, M. Ikeda, H. Kuwabara, T. Yui, *J. Am. Chem. Soc.* **2007**, *129*, 15732.
[73] C. Niebel, Y. Kim, C. Ruzié, J. Karpinska, B. Chattopadhyay, G. Schweicher, A. Richard, V. Lemaur, Y. Olivier, J. Cornil, A. R. Kennedy, Y. Diao, W.-Y. Lee, S. Mannsfeld, Z. Bao, Y. H. Geerts, *J. Mater. Chem. C* **2015**, *3*, 674.
[74] B. E. Sørensen, *Eur. J. Mineral.* **2013**, *25*, 5.
[75] A. Lempel, J. Ziv, *IEEE Trans. Inf. Theory* **1976**, *22*, 75.